The Astrophysical Journal, 673:1181–1187, 2008 February 1

HARD X-RAY EMISSIONS FROM PARTIALLY OCCULTED SOLAR FLARES

Säm Krucker[1] and R. P. Lin[1,2]
krucker@ssl.berkeley.edu
Received 2007 August 10; accepted 2007 September 22

ABSTRACT

Observations of solar flares partially occulted by the solar limb provide diagnostics of coronal hard X-ray (HXR) emissions in the absence of generally much brighter emissions from footpoints of flare loops. In this paper, a statistical survey of 55 partially occulted flares observed by the *Reuven Ramaty High-Energy Solar Spectroscopic Imager* (*RHESSI*) is presented, revealing the existence of two different components of coronal HXR emissions. Below ∼15 keV thermal HXR emission with a gradual time profile is generally dominant, while at higher energies an additional component is seen in 50 out of 55 events. This additional component shows faster time variations in the order of tens of seconds and is most prominent during the rise of the thermal emission. A comparison of the centroid positions of these two emissions shows that they are most often cospatial within ∼2000 km, although for a few events clear separations are observed as well. The spectra of the high-energy component show a rather steep (soft) power law with indices mostly between ∼4 and ∼6. Thin target emission in the corona from flare-accelerated electrons is discussed as a possible origin of the fast time variation component.

Subject headings: Sun: flares — Sun: particle emission — Sun: X-rays, gamma rays

1. INTRODUCTION

Particle acceleration during solar flares is observed to be surprisingly efficient, as flare-accelerated energetic particles contain a significant fraction of the total energy released. The mechanisms that accelerate these particles are not understood. Collisions between flare-accelerated electrons and the ambient plasma produce hard X-ray emissions (nonthermal bremsstrahlung), allowing in principle the tracing of energetic electrons in the corona. However, the intensity of nonthermal bremsstrahlung emissions depends on the ambient plasma density, and since the density increases very rapidly in the transition region, HXR emissions are most prominent from footpoints of flare loops. Nonthermal bremsstrahlung emissions produced by flare-accelerated electrons in the corona are much weaker, as the densities are generally much lower. In a few cases coronal densities seem to be high enough and flare-accelerated electrons are already stopped in the corona (especially if the flare-accelerated electrons have very flat spectra), and HXR sources are dominantly seen in the corona (Veronig & Brown 2004). In most flares, however, the limited dynamic range of HXR imaging observations makes it impossible to observe coronal HXR emissions from the same electrons that later lose their energy in HXR footpoints. Nevertheless, a few examples are reported that clearly show HXR emissions from coronal sources (Frost & Dennis 1971; Roy & Datlowe 1975; McKenzie 1975; Hudson 1978; Kane et al. 1992; Masuda et al. 1994; Mariska et al. 1996; Tomczak 1997, 2001; Sato 2001; Hudson et al. 2001; Petrosian et al. 2002; Battaglia & Benz 2006; Asai et al. 2007; Krucker et al. 2007,). The most prominent example, the Masuda flare, shows next to HXR footpoint emissions a third HXR source ∼10″ above the thermal loops seen in soft X-rays (Masuda et al. 1994). This third source shows an impulsive temporal profile and a nonthermal spectrum during the peak with a power-law index of around ∼4 above 22 keV, but is most likely produced by a different population of electrons than the electrons losing their energy in the HXR footpoints (Alexander & Metcalf 1997).

For flares occurring a few degrees or more behind the solar limb, HXR footpoints are occulted and coronal emissions can be observed without being limited by the dynamic range of HXR imaging observations. A statistical survey of partially occulted flares observed by *Yohkoh* reveals the existence of coronal HXR emissions besides the main thermal sources in most events (Tomczak 2001), but the limited energy resolution of *Yohkoh*/HXT makes it often difficult to separate an additional component at high energy from the main thermal emission. The relative source location of the coronal HXR emission is found to be only slightly displaced (<5″) from the thermal emission in all cases except the Masuda flare (Tomczak 2001; Petrosian et al. 2002).

Observations with *RHESSI* (Lin et al. 2002) provide for the first time imaging spectroscopy with good spectral (∼1 keV) and spatial (∼2″) resolution. Battaglia & Benz (2006) analyzed five *RHESSI* flares with coronal sources well separated from the related HXR footpoint emissions, finding, in addition to thermal emissions, faint HXR emissions with a soft power-law spectra in the corona. In this paper a statistical survey of *RHESSI* flares with occulted HXR footpoints is investigated, and statistical results of temporal, spatial, and spectral behavior are presented.

2. OBSERVATIONS AND DATA ANALYSIS

The 55 partially occulted flares presented in this survey are selected from the *RHESSI* flare list from 2002 February to 2004 August. In a first step, the automatically determined flare location of the *RHESSI* flare list is used to find flares occurring above the solar limb. In a second step, visual inspection of images in the thermal range and at higher energies is used to only select flares without HXR footpoint emissions (i.e., flares showing HXR footpoint emissions right above the limb and thermal emissions from the corona are not selected). Since for technical reasons the automated imaging algorithm of the *RHESSI* flare list does not always provides a flare location, the list of partially occulted flares is not complete, but should not contain selection biases, except that only the larger events with *GOES* SXR flare classifications

[1] Space Sciences Laboratory, University of California, Berkeley, CA 94720-7450.
[2] Department of Physics, University of California, Berkeley, CA 94720-7300.

TABLE 1
PARTIALLY LIMB-OCCULTED *RHESSI* FLARES

Date	*GOES* Peak Time	*GOES* Class	Location	Break Energy (keV)	γ
2002 Mar 7	17:51	C2.5	East S10	~16	~3.7
2002 Mar 28	17:58	C7.6	West S03	~19	~5.7
2002 Apr 4	10:45	M1.4	East S19	~22	~5.5
2002 Apr 4	15:29	M6.1	East S18	~25	~4.5
2002 Apr 18	06:42	C9.4	West N18	~18	~5.3
2002 Apr 22	12:05	C2.8	West S18	~16	~3.7
2002 Apr 29	13:00	C2.2	East S18	~13	~7.9
2002 Apr 30	00:33	C7.8	East S21	~19	~5.4
2002 Apr 30	08:20	M1.3	East S20	~21	~5.7
2002 May 17	02:01	C5.0	East N13	~19	~4.6
2002 May 17	07:38	M1.5	East N14	~23	~6.6
2002 Jul 5	08:04	C7.8	West S17	~19	~7.9
2002 Jul 6	03:34	M1.8	West S16	~19	~6.2
2002 Jul 8	09:17	M1.6	East N19	~18	~5.6
2002 Jul 9	04:11	C8.6	West N19	~16	~4.1
2002 Aug 4	09:38	M6.6	West S19	~19	~7.5
2002 Aug 4	14:14	C6.9	West S17		
2002 Aug 28	18:57	M4.6	East N09	~23	~3.4
2002 Aug 28	21:44	M1.1	West S24	~26	~4.6
2002 Aug 29	02:51	M1.6	East N09	~23	~4.9
2002 Aug 29	05:44	M1.8	East N08	~22	~5.1
2002 Sep 6	16:27	C9.2	East S05	~23	~3.9
2002 Oct 16	16:00	C6.5	East N27	~19	~6.1
2002 Nov 15	01:08	M2.4	East S16	~18	~5.8
2002 Nov 23	01:24	C2.1	East N13	~27	~4.2
2003 Jan 21	01:25	C2.0	East S16		
2003 Feb 1	08:58	M1.2	East S14	~27	~4.4
2003 Feb 1	19:46	C5.0	East S13	~17	~7.3
2003 Feb 14	09:17	M1.2	West N11	~20	~5.9
2003 Mar 27	14:54	C2.3	West N17	~22	~5.9
2003 Apr 24	04:54	C7.1	West N15	~19	~6.1
2003 Apr 24	06:35	C1.0	West N15	~20	~3.7
2003 May 7	20:47	C5.9	East N14	~29	~5.0
2003 Jun 1	12:48	M1.0	East N10	~22	~3.9
2003 Jun 2	08:15	M3.9	West S08	~21	~4.2
2003 Jun 6	16:13	C2.5	East S14	~20	~4.8
2003 Aug 21	15:19	C4.9	West S09	~25	~4.1
2003 Sep 15	16:39	C1.5	West S06		
2003 Sep 29	16:09	C5.1	East S08		
2003 Oct 21	23:16	M2.3	East S15	~26	~6.4
2003 Oct 22	18:43	C6.0	East S16	~20	~5.1
2003 Oct 22	21:58	M2.1	East S15	~23	~5.7
2003 Oct 23	00:58	C7.0	East S16		
2003 Nov 4	14:47	C9.0	West N10	~19	~6.8
2003 Nov 4	15:30	C7.0	West N10	~16	~4.7
2003 Nov 5	01:59	M1.6	West N09	~21	~6.3
2003 Nov 18	09:53	M4.5	East S13	~18	~5.6
2003 Nov 18	22:17	C6.1	East S15	~27	~3.7
2003 Nov 19	10:07	C4.9	East S16	~17	~4.9
2004 Mar 5	08:55	C6.6	East S16	~21	~5.6
2004 Mar 24	23:28	M1.5	East N14	~22	~6.7
2004 Jul 15	22:27	C7.9	East N10	~22	~7.6
2004 Jul 17	03:46	C4.2	East N08	~24	~4.6
2004 Aug 18	08:41	C6.0	West S12	~27	~6.4
2004 Aug 19	06:57	M3.0	West S12	~27	~6.7

from C1 to M6 (22 M-class flares, 33 C-class flares) are selected. This paper presents a representative survey of partially limb-occulted flares with HXR footpoints occulted and the main thermal flare loops visible (Table 1). Events for which the main thermal flare loops are occulted as well (Kane et al. 1992; Krucker et al. 2007), however, are not included in this survey, as these events have generally much smaller thermal emissions (B class and below) than the events selected here.

2.1. *Time Profiles*

The excellent spectral resolution of *RHESSI* (~1 keV) allows us to separate thermal HXR emissions from emissions at high

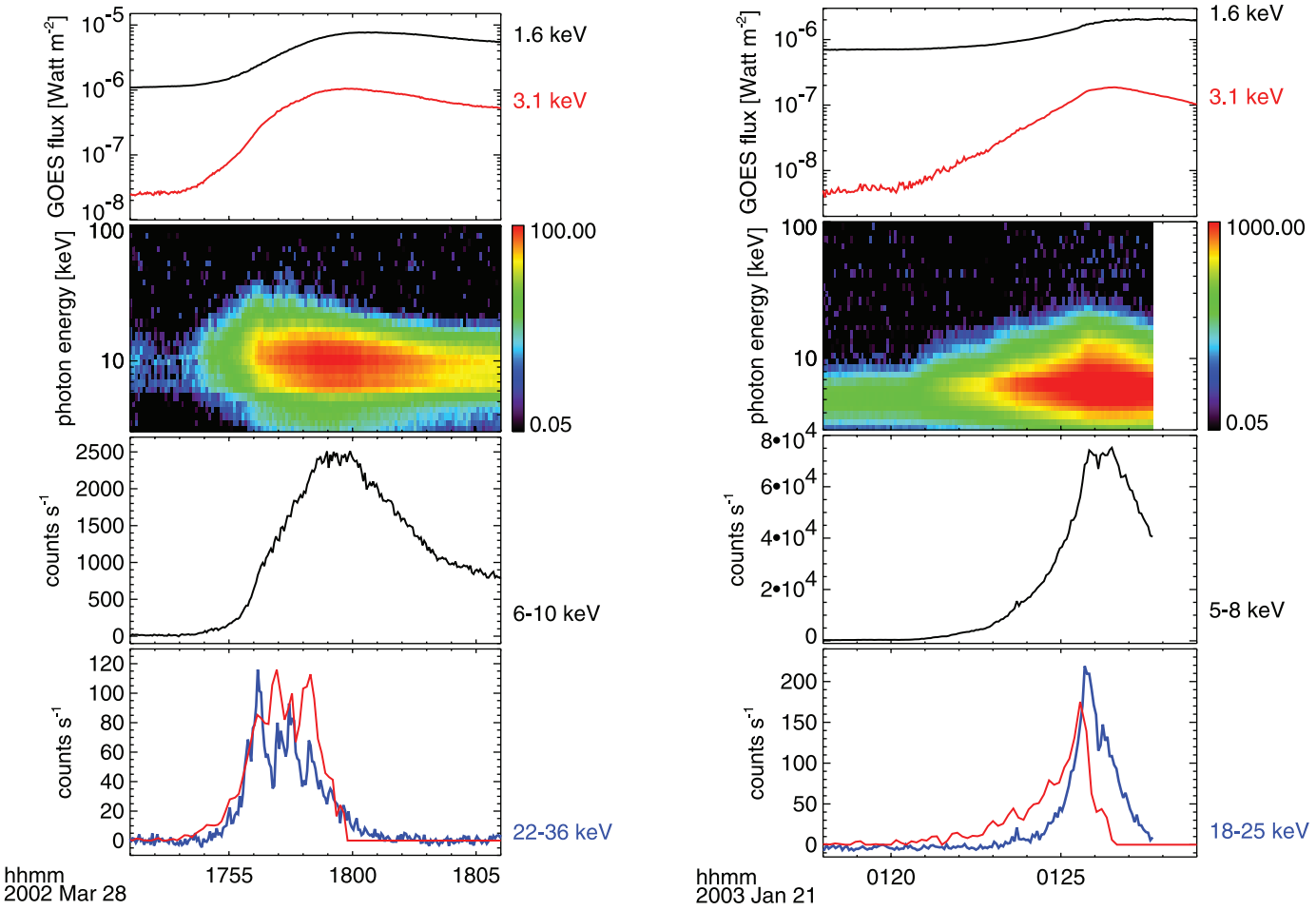

FIG. 1.—Examples of X-ray time profiles of two partially occulted flares. From top to bottom, the panels show *GOES* SXR time profiles, *RHESSI* spectrogram plots, time profiles of the thermal X-ray emission, and time profiles at higher energies (*blue*). The panels at the bottom also show the derivative of the high-energy *GOES* light curve (*red*) in arbitrary units. *Left*: Typical example (50 of 55 events) with fast time variations at high energies; *right*: flare with gradual time variation at higher energies similar to the thermal emission at lower energies (note that the large difference in count rate at lower energies between the two flares is because of the different attenuator state at the time of the observations).

energies, and allows us therefore to systematically search for faint nonthermal emissions above the main thermal contribution. To study temporal evolution at different energies, two energy ranges are selected. An energy range clearly in the thermal range (different for each event, but generally below ~15 keV) and the second energy range at higher energies (generally from ~20 keV up to the maximum energy with counts above the instrumental background) are selected with the help of the spectral fitting results from § 2.3.

Although thermal HXR emissions seen by *RHESSI* are generally produced by higher temperature flare plasmas than the *GOES* SXR emission (e.g., Holman et al. 2003), the thermal profiles in HXR and SXR are similar, with rather gradual time variations (Fig. 1). The time profiles at higher energies, on the other hand, generally (50 out of 55 events) show a clearly different temporal behavior from the thermal emissions, with faster variations and multiple peaks with duration of tens of seconds (Fig. 1, *left*). Furthermore, the fast time variation emissions tend to be most prominent during the rise of the thermal emission and roughly correspond to the time variations seen in the derivative of the *GOES* soft X-ray light, reminiscent of the Neupert effect (Neupert 1968). The other five events show similar time profiles at all energies, but tend to be smaller flares with *GOES* classes below C7, and the fast time variation component could possibly be hidden in the noise of the observations.

2.2. *Imaging*

Detailed X-ray imaging of each flare is not the goal of this initial survey. In a first attempt to quantify the relative location of the thermal component and the component with fast time variations, the source centroid positions are determined at the two selected energy ranges by fitting a single Gaussian source to the *RHESSI* visibilities (Schmahl et al. 2007). Fitting only a single Gaussian does not provide details of the X-ray source structure, but it gives reliable estimates of centroid positions (center of mass positions) and source sizes. To enhance counting statistics, the determined source centroids are averaged over the duration of the fast time variation emission (typically ~2 minutes). As a check, images reconstructed with the CLEAN algorithm (Hurford et al. 2002) at 12″ resolution FWHM integrated over the same time interval are used as well to get centroid positions.

Figure 2 (*bottom right*) shows the histogram of the spatial separation of the thermal emissions and the emissions with the fast time variation. The bin size of 1″ is roughly equal to uncertainties in the derived centroid positions given by the forward fitting method. The difference in the two histograms is because

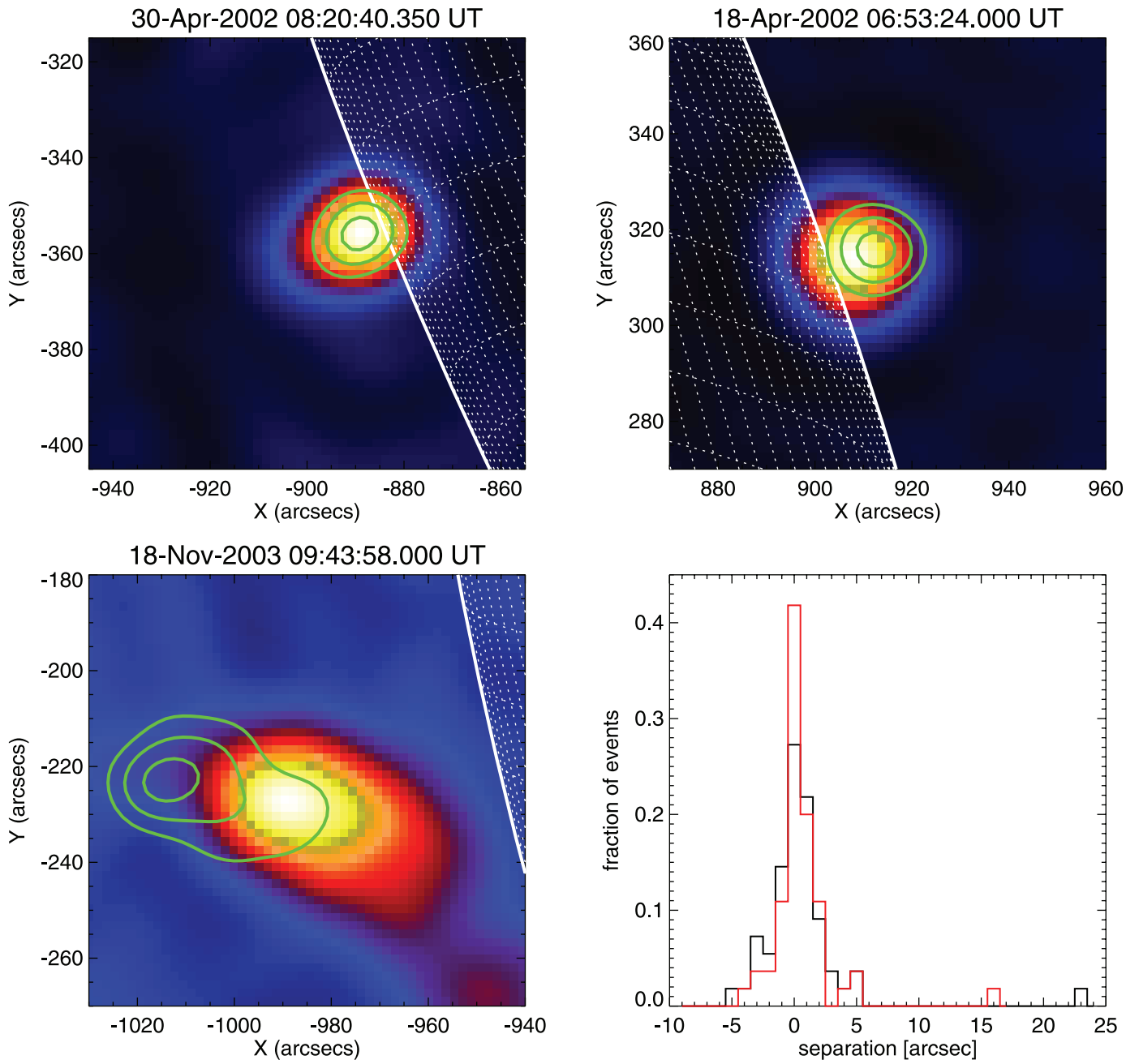

FIG. 2.—Example of imaging in the thermal range and at higher energies. The images show maps reconstructed with the CLEAN algorithm (field of view of 90″) in the thermal range (typically 6–12 keV, but slightly different for each event) and green contours at higher energies (typically 20–30 keV) with levels 50%, 70%, 90%. *Top left*: Event with cospatial emissions at both energy ranges; *top right*: event with a ~5″ separation; *bottom left*: event with the largest separation in the survey. At the bottom right the histogram of the radial separation of the thermal component, and the component with high time variation is shown revealing that most of the events are cospatial. The red histogram represents the radial difference of the center of mass locations, the black histogram shows the radial difference between the locations of the maximum intensity of the images reconstructed with the CLEAN algorithm.

the forward fit results only reflects the center-of-mass locations, while the maps reconstructed with the CLEAN algorithm sometimes show asymmetric sources with a peak location slightly different from the center-of-mass location (best seen for the event presented in Fig. 2, *bottom left*). The histograms clearly show that most of the fast time variation emissions are cospatial within a few arcseconds with the thermal emissions, and only a few events show clear spatial separation. However, since only center-of-mass locations are considered here, this does not exclude different source shapes. Compared to the above-the-loop-top source seen in the Masuda flare, all but one of the flares have smaller separations by a factor of 2 or more. These findings are consistent with statistical studies of partially occulted flares observed by *Yohkoh* (Tomczak 2001) reporting cospatial emission at SXR and HXR wavelengths for half of the flare, and separations below 5″ for the other half. Since the Tomczak study makes a comparison relative to the thermal emissions seen in SXR and not HXR as in this survey, the difference reported here is expected to likely be a bit smaller, since SXR flare loops are generally seen below the HXR flare loops (e.g., Gallagher et al. 2002). Detailed X-ray imaging at higher spatial resolution in combination with imaging at other wavelengths is the next step in spatial data analysis of this set of events and will be published in a separate paper.

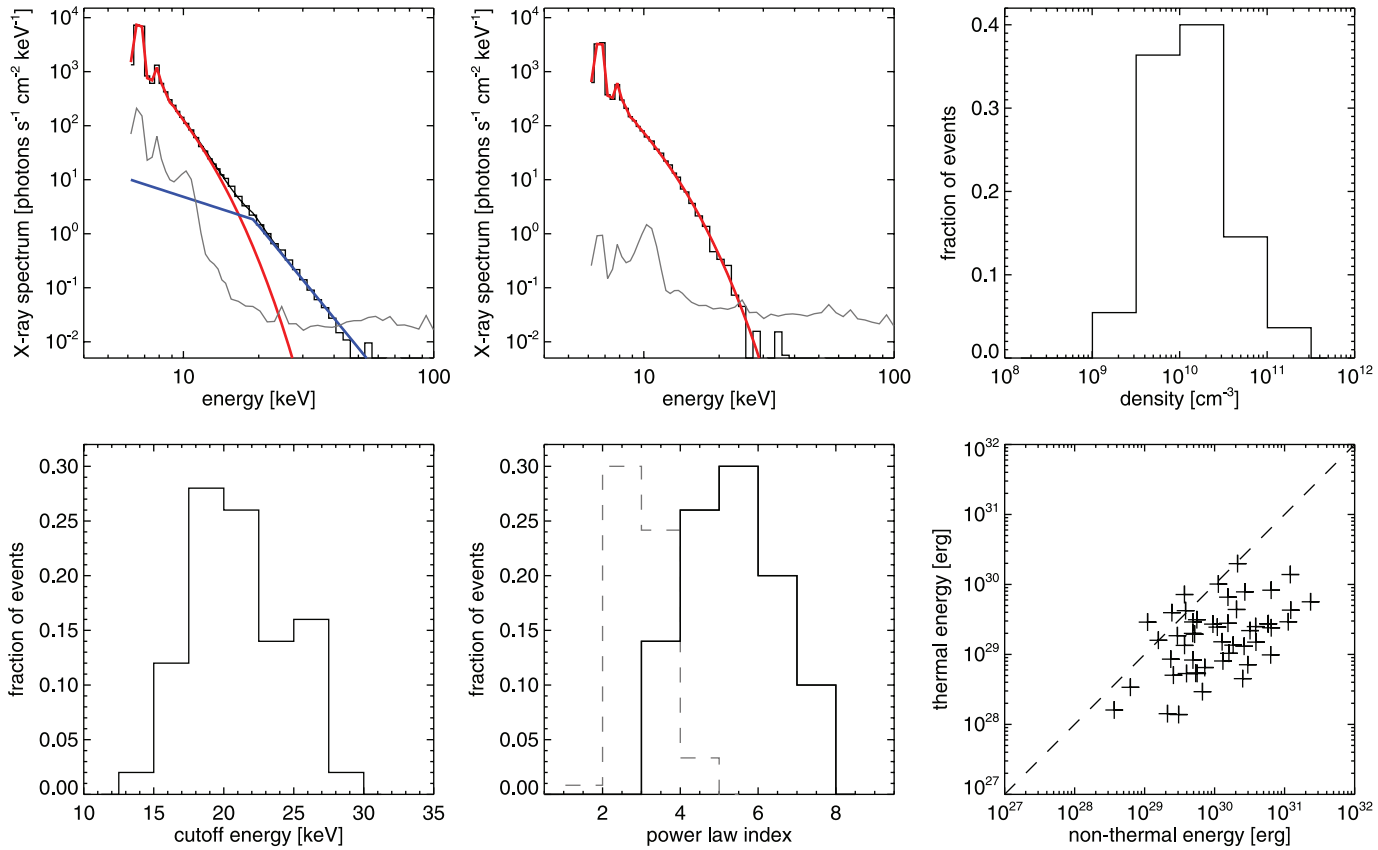

FIG. 3.—Spectral fitting results. *Top left*: Example of photon spectral fitting for the partially occulted flare on 2002 March 28 (17 : 55:58–17 : 56:18 UT) shown in Fig. 1. The background subtracted data is shown in black and the background in gray. The thermal fit is given in red (temperature of 24 MK), and the broken power-law fit in blue (with break energy around 19 keV and power-law index of 5.7 ± 0.2). *Top middle*: Similar plot for the mostly thermal event shown in Fig. 1. *Top right*: Histogram of derived densities of the thermal source. *Bottom left*: Histogram of the cutoff energies in the photon spectrum. *Bottom middle*: Histogram of the power-law indices. For comparison, the histogram for a sample of on-disk flare from Saint-Hilaire et al. (2007) is shown in dashed gray. *Bottom right*: Correlation plot between the thermal energy in the flare loop and nonthermal energy in energetic electrons above 20 keV for the 50 events with fast time variation emission. The nonthermal energy is derived assuming the observed HXR emission is produced in thin target approximation and electrons are leaving the coronal source without being trapped and deposit their energy in the occulted HXR footpoints. The dashed line represents equal energy in the thermal and nonthermal population. Since systematic errors dominate, all values shown are order of magnitude approximations, and no error bars are given. Nevertheless, a rough correlation is seen.

2.3. *Spectra*

Spectral fitting is done during the peak ($\sim$20 s interval) of the fast time variation component using standard *RHESSI* software. A thermal component and a broken power law with a fixed slope of 1.5 below the break (e.g., Emslie 2003) represents the data reasonably well (Fig. 3, *top left*), except in the five cases without a fast time variation component (in Table 1, no values for the spectral fitting are given for these events), where only a single thermal fit is needed (Fig. 3, *top middle*). Below $\sim$15 keV, thermal emissions generally dominate, with emission measures between $\sim 10^{46}$ and $\sim 10^{49}$ cm^{-3} and temperatures between $\sim$20 and $\sim$40 MK. Above $\sim$15 keV, the spectrum deviates from a single thermal fit (except for the five events mentioned earlier) and can be represented with a steep power-law spectra, with indices γ between $\sim$4 and $\sim$7 (Fig. 3, *bottom middle*). A recent statistical study of photon spectral indices of *RHESSI* flares of similar sizes occurring on the solar disk (Saint-Hilaire et al. 2007) gives much harder spectra with values of γ between $\sim$2 and $\sim$4. Since the spectra of the coronal source with fast time variations are relatively soft, they can also be fitted with further thermal components. Generally, a total of three isothermal components are needed to get a good representation of the observations with temperatures up to $\sim$100 MK and rather small emission measures (typically 10^{-4} of main thermal emission). Figure 4 shows an example comparing thermal and power-law fits with a triple thermal fit. Both fits represent the data well, with χ^2 of 0.9 and 1.1 for the examples shown in Figure 4, respectively, and the residuals of both fits are evenly distributed. A double temperature fit does not represent the data well, showing systematic deviations in the residuals, and generally gives larger χ^2. The fitting results do not favor either a power-law (e.g., nonthermal fit) or a thermal fit; however, the power-law fit only uses five parameters to fit the data compared to six parameters for the triple thermal fit.

The main thermal fits, together with the source sizes derived from imaging, gives an order-of-magnitude estimate of the coronal flare densities (at the time of the fast time variations), with most of the densities between $\sim 5 \times 10^9$ and $\sim 5 \times 10^{10}$ cm^{-3}, assuming a filling factor of the order of unity. (Fig. 3, *top right*). Using these densities, the column density in the thermal source can be calculated giving values between $\sim 10^{18}$ and $\sim 10^{19}$ cm^{-2}. These column densities N can stop electrons with energy $E_{\rm stop} = (10^{-17}N)^{1/2}$, i.e., between 3 and 10 keV. Hence, the derived coronal densities are not high enough to efficiently stop energetic electrons, and the fast time variation component is therefore more likely produced in a thin target scenario, at least for a filling factor of order of unity and in the absence of electron trapping.

3. DISCUSSION AND SUMMARY

This paper presents a survey of 55 partially occulted limb flares observed by *RHESSI* in X-rays above 3 keV. Next to thermal

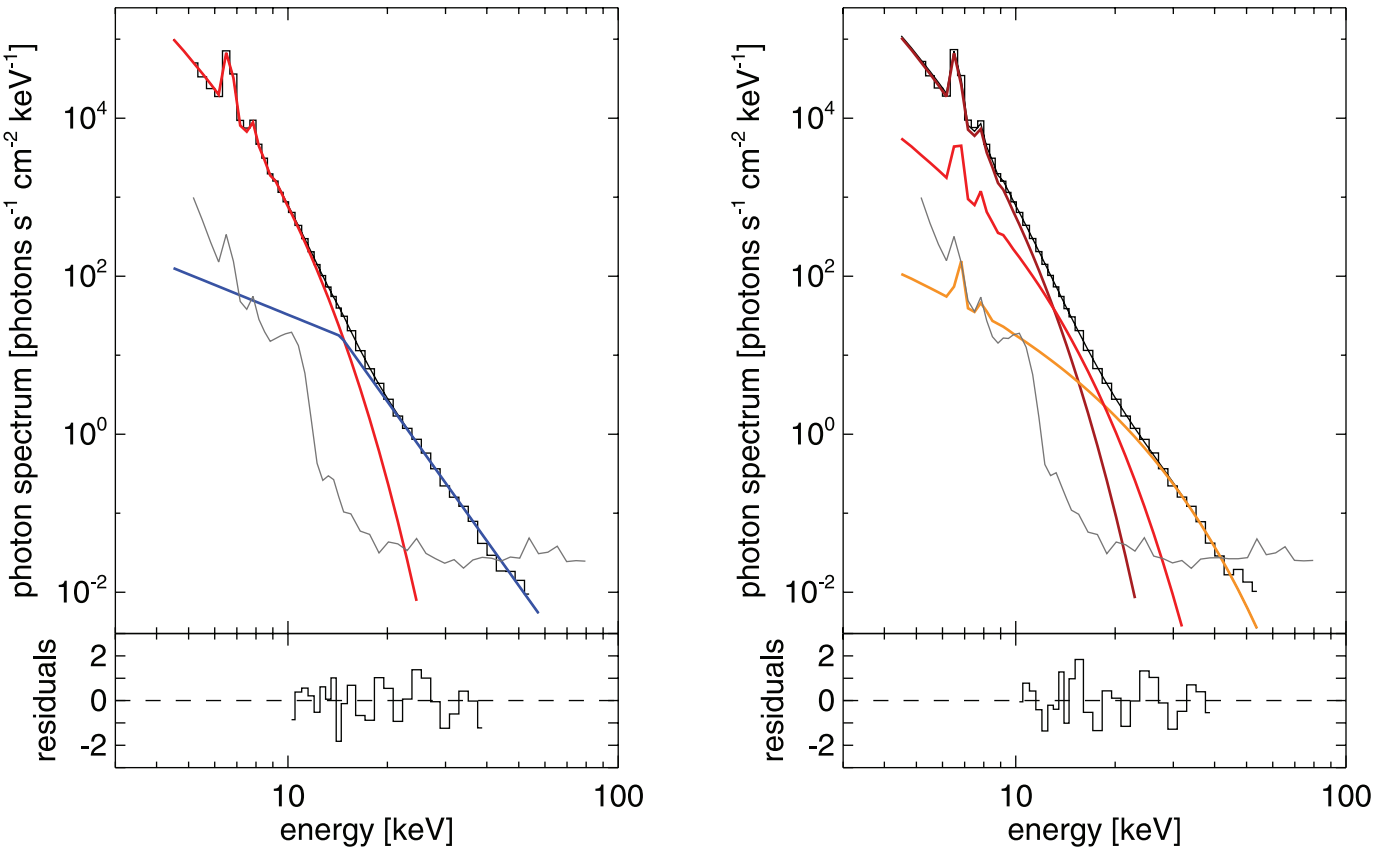

FIG. 4.—Two different spectral fits to the data taken during the 2003 November 18 flare between 09:43:03 and 09:43:16 UT. The data are shown as histograms, while the sum of all fitted components is the solid black line. The residuals of the fit in units of the standard deviation derived from photon statistics is shown on the bottom panel. *Left*: A thermal fit (*red*) plus a broken power-law fit with a fixed slope of 1.5 below the break (*blue*) gives $T \sim 16$ MK, EM $\sim 1 \times 10^{49}$ cm^{-3}, a break around ~14 keV, and a power-law index of 6.0. *Right*: Three thermal fits (*three different shades of red*) with temperatures of $T_1 \sim 15$ MK, $T_2 \sim 30$ MK, and $T_3 \sim 88$ MK and emission measures of EM$_1 \sim 1 \times 10^{49}$ cm^{-3}, EM$_2 \sim 9 \times 10^{46}$ cm^{-3}, and EM$_3 \sim 1 \times 10^{45}$ cm^{-3}.

emissions from the corona, a second component with fast time variations best seen above ~20 keV is observed in most of the events (50 out of 55). The second component is most prominent during the rise phase of the thermal emission, has a much softer spectrum than spectra of on-disk flares, and its centroid position is often cospatial or within a few arcsec of the thermal emission. These results are consistent with *Yohkoh*/HXR survey of partially occulted flares by Tomczak (2001), and highlight again how unusual the above-the-loop top source in the Masuda flare is.

HXR emissions from on-disk flares, where most of the emission originates from footpoints of flare loops, also show fast time variations, and they also occur mostly prominently during the rise of the thermal emission. This suggests that the observed coronal HXR emissions might be produced by the same population of electrons that generally produce HXR footpoint emissions in the chromosphere. Since the derived coronal densities are relatively low (Fig. 3, *top right*), flare-accelerated electrons are not losing a significant amount of energy in the corona, and emit only faint HXR emissions with a soft spectrum in the thin-target approximation (Brown 1971; Lin 1974). Assuming the electron spectra with a power-law shape, the thin-target model predicts power-law photon spectra with indices of 2 higher (steeper) than the thick target model. Comparing the histograms for the partially occulted events with the on-disk events (Fig. 3, *bottom middle*), a difference in power-law indices of 2 seems to be possible. Imaging spectroscopy results of five *RHESSI* flares by Battaglia & Benz (2006) also clearly show soft spectra for the coronal sources; however, the power-law indices of footpoints and coronal sources can differ from 2, indicating that a simple thin-thick target model does not work for all events. Noncollisional losses (e.g., deceleration in electric fields due to return currents) relevant for the precipitating electrons only, could produce differences larger than 2 (Battaglia & Benz 2007).

The instantaneous energy rate in nonthermal electrons needed to produce the observed HXR emissions in the thin target approximation is straightforward to derive (Brown 1971; Lin 1974), but depends on the not well known cutoff energy in the electron spectrum. The total energy in nonthermal electrons can then be calculated by considering how long electrons stay in the corona and how long the HXR emissions last. The shorter the electrons stay in the corona the larger the number of electrons needed (with the transit time through the thermal source giving the shortest time electrons stay in the corona). Assuming a cutoff energy of ~20 keV and using the transit time of 20 keV electrons through the thermal source, the derived total energies in nonthermal electrons are between 10^{29} and 10^{31} ergs. If electrons are trapped, the nonthermal energy required can be lower. Electrons radiating HXRs in the thin-target approximation in the corona do not lose a significant amount of energy, but they later deposit all their energy in the occulted footpoints in the chromosphere and heat the flare loop by chromospheric evaporation. Figure 3 (*bottom right*) shows the thermal energy of the coronal source as a function of the derived nonthermal energy. Despite the fact that these values are only order-of-magnitude approximations, a rough correlation is seen. The nonthermal energy, E_{nt}, heavily depends on the cut-off

electron energy, E_0, and the time, τ, the electrons spend in the corona: $E_{\rm nt} \propto \tau^{-1} E_0^{-\gamma+1}$. However, for reasonable parameters of E_0 (the cutoff energy in the photon spectrum limits E_0) and τ (τ cannot be too large, otherwise the thin target approximation breaks down), the nonthermal energy tends to be similar to or larger than the thermal energy, similar to what is found for energy estimates from spectral analysis of on-disk flares (e.g., Saint-Hilaire & Benz 2005). This rough comparison shows that it is possible that the fast time variation component is thin-target emission from the main flare-accelerated electrons that later lose their energy in the flare loop footpoints. However, other scenarios cannot be excluded. The few events with hard spectra ($\gamma < 4$) are more likely produced in a thick or partially thick target and might be different kinds of events, and trapping of electrons is likely important. Events with a very clear spatial separation between the thermal and fast time variation emission are likely also a different class of events. Furthermore, a thermal interpretation of the fast time variation component cannot be excluded either. The fast time variations would indicate heating and cooling on similar timescales of tens of seconds. Adiabatic compression of coronal plasma (adiabatic compression heats the plasma, and relaxation cools it) could produce the observed HXR emissions without the need of energetic electrons (Maetzler et al. 1978), but the nature of the compression is unclear.

The next step of data analysis includes detailed and time-dependent X-ray imaging with the full capability of *RHESSI* and comparing the details of the X-ray source structures with imaging observations at other wavelengths. First results of a single-event analysis combining *RHESSI* and *Hinode* X-ray observations support the thin-target interpretation (Krucker et al. 2007). Future statistical analysis will provide further tests of the thin-target emission scenario and the adiabatic compression idea (HXR source size should anticorrelate with HXR flux in time), and will reveal the nature of events with a clear spatial separation.

The work was supported through NASA contract NAS 5-98033 for *RHESSI*. S. K. would like to thank Alicia Chavier for the help with the final draft and the International Space Science Institute, Bern, Switzerland for supporting the working group on "Coronal Hard X-ray Sources in Solar Flares."

REFERENCES

Alexander, D., & Metcalf, T. R. 1997, ApJ, 489, 442
Asai, A., Nakajima, H., Oka, M., Nishida, K., & Tanaka, Y. T. 2007, Adv. Space Res., 39, 1398
Battaglia, M., & Benz, A. O. 2006, A&A, 456, 751
———. 2007, A&A, 466, 713
Brown, J. C. 1971, Sol. Phys., 18, 489
Emslie, A. G. 2003, ApJ, 595, L119
Frost, K. J., & Dennis, B. R. 1971, ApJ, 165, 655
Gallagher, P. T., Dennis, B. R., Krucker, S., Schwartz, R. A., & Tolbert, A. K. 2002, Sol. Phys., 210, 341
Holman, G. D., Sui, L., Schwartz, R. A., & Emslie, A. G. 2003, ApJ, 595, L97
Hudson, H. S. 1978, ApJ, 224, 235
Hudson, H. S., Kosugi, T., Nitta, N. V., & Shimojo, M. 2001, ApJ, 561, L211
Hurford, G. J., et al. 2002, Sol. Phys., 210, 61
Kane, S. R., McTiernan, J., Loran, J., Fenimore, E. E., Klebesadel, R. W., & Laros, J. G. 1992, ApJ, 390, 687
Krucker, S., Hannah, I. G., & Lin, R. P. 2007, ApJ, 671, L193
Krucker, S., White, S. M., & Lin, R. P. 2007, ApJ, 669, L49
Lin, R. P. 1974, Space Sci. Rev., 16, 189
Lin, R. P., et al. 2002, Sol. Phys., 210, 3
Maetzler, C., Bai, T., Crannell, C. J., & Frost, K. J. 1978, ApJ, 223, 1058
Mariska, J. T., Sakao, T., & Bentley, R. D. 1996, ApJ, 459, 815
Masuda, S., Kosugi, T., Hara, H., Tsuneta, S., & Ogawara, Y. 1994, Nature, 371, 495
McKenzie, D. L. 1975, Sol. Phys., 40, 183
Neupert, W. M. 1968, ApJ, 153, L59
Petrosian, V., Donaghy, T. Q., & McTiernan, J. M. 2002, ApJ, 569, 459
Roy, J.-R., & Datlowe, D. W. 1975, Sol. Phys., 40, 165
Saint-Hilaire, P., & Benz, A. O. 2005, A&A, 435, 743
Saint-Hilaire, P., Krucker, S., & Lin, R. P. 2007, Sol. Phys., submitted
Sato, J. 2001, ApJ, 558, L137
Schmahl, E. J., Pernak, R. L., Hurford, G. J., Lee, J., & Bong, S. 2007, Sol. Phys., 240, 241
Tomczak, M. 1997, A&A, 317, 223
———. 2001, A&A, 366, 294
Veronig, A. M., & Brown, J. C. 2004, ApJ, 603, L117